


Symmetry-protected Dirac nodal lines and large spin Hall effect in a V_6Sb_4 kagome bilayerY. Yang,¹ R. Wang^{1,2,3,4,*}, M.-Z. Shi,¹ Z. Wang,^{1,5} Z. Xiang,¹ and X.-H. Chen^{1,5,6,7}¹CAS Key Laboratory of Strongly-coupled Quantum Matter Physics, Department of Physics, University of Science and Technology of China, Hefei, Anhui 230026, China²Institute for Structure and Function & Department of Physics, Chongqing University, Chongqing 400044, China³Center of Quantum Materials and Devices, Chongqing University, Chongqing 400044, China⁴Chongqing Key Laboratory for Strongly Coupled Physics, Chongqing University, Chongqing 400044, China⁵CAS Center for Excellence in Superconducting Electronics (CENSE), Shanghai 200050, China⁶CAS Center for Excellence in Quantum Information and Quantum Physics, Hefei, Anhui 230026, China⁷Collaborative Innovation Center of Advanced Microstructures, Nanjing University, Nanjing 210093, China (Received 21 December 2021; revised 15 March 2022; accepted 23 March 2022; published 1 April 2022)

Recently, a family of nonmagnetic kagome metals AV_3Sb_5 ($A=K, Rb,$ and Cs) has attracted significant attention for realizing the intertwining of quantum order and nontrivial topology. However, these compounds have been identified to host complex band structures. Therefore, it is desirable to design and synthesize novel kagome materials with a simple band topology and good transport properties. In this study, using first-principles calculations, we present the electronic properties and the intrinsic spin Hall effect of V_6Sb_4 , the latest experimentally synthesized vanadium-based compounds that form a kagome bilayer. In the absence of spin-orbital coupling (SOC), this compound is a Dirac nodal line semimetal with symmetry-protected nodal rings near the Fermi level. Within the SOC, the spin-rotation symmetry breaks the gaps of the nodal rings with a small band gap. Furthermore, based on the Wannier tight-binding approach and the Kubo formula, we reveal a large spin Hall effect in V_6Sb_4 , which intrinsically originates from the spin Berry curvature. Our work further expands nonmagnetic kagome compounds for applications in spintronics accompanied by exotic quantum order.

DOI: [10.1103/PhysRevB.105.155102](https://doi.org/10.1103/PhysRevB.105.155102)**I. INTRODUCTION**

Materials with a kagome lattice have attracted significant interest in condensed matter physics owing to their unusual lattice geometry. The kagome lattice possesses a two-dimensional (2D) corner-sharing triangular network, which ensures that its band structure uniquely exhibits the coexistence of linear Dirac and flat bands. Consequently, numerous topological and many-body quantum phenomena have been identified over the past decade, such as charge density waves (CDWs) [1], bond density wave order [2,3], charge fractionalization [4], quantum limit–Chern topological phases [5], quantum spin-liquid states [6,7], and topological superconductivity [8]. These findings strengthen the understanding of correlated band topology.

Recently, the discovery of a new family of nonmagnetic kagome metals AV_3Sb_5 ($A=K, Rb,$ and Cs) further promoted the development of exotic physics in kagome lattices [9–18]. These compounds have a superconducting ground state intertwined with the CDW order [11,12,14]. Theoretical calculations have shown that the normal state of these compounds has been categorized as a \mathbb{Z}_2 topological metal. More strikingly, intense studies have been conducted to reveal the close correlations between superconductivity, CDW, and nontrivial band topology in AV_3Sb_5 [15,16,19–21], pushing this topic to the quantum frontier. Beyond the acquisition of

promising quantum phenomena in AV_3Sb_5 , of equal importance is the exploration of more kagome materials, which will further lead to the experimental realization of rich phenomena between band topology and quantum ordered states. Additionally, the complicated Fermi surface topology of AV_3Sb_5 , such as multiple trivial and nontrivial bands across the Fermi level, would make the understanding of transport properties ambiguous. For instance, a giant anomalous Hall effect in the absence of a magnetic order was observed at low temperatures [22,23], but the mechanism remained unclear [24,25]. Therefore, the design and synthesis of novel kagome materials with ideal band topologies and good transport properties are desirable.

The AV_3Sb_5 compounds crystallize in a layered structure with a prototypical kagome V_3Sb monolayer, which dominates the electronic and topological properties [9]. However, to the best of our knowledge, vanadium-based materials that form a kagome bilayer or beyond have rarely been reported in the literature. Recently, our group discovered two members of vanadium compounds that form a $(V_3Sb)_2$ kagome bilayer in their crystal structures with the space group $R\bar{3}m$ (No. 166), such as AV_6Sb_6 and V_6Sb_4 [26]. Importantly, these two members and AV_3Sb_5 can be represented as a generic chemical formula $A_{m-1}Sb_{2m}(V_3Sb)_n$ (i.e., AV_3Sb_5 with $m=2, n=1$; AV_6Sb_6 with $m=2, n=2$; V_6Sb_4 with $m=1, n=2$). Importantly, we demonstrated that AV_6Sb_6 compounds host exotic type-II nodal lines adjacent to the Fermi level and superconductivity under pressure [26,27], implying that vanadium-based kagome bilayer compounds could potentially

*rcwang@cqu.edu.cn

be viewed as ideal candidates for studying exotic quantum phenomena with unconventional fermionic excitations.

In this work, using first-principles calculations, we investigated the band topology and its induced intrinsic spin Hall effect (SHE) of V_6Sb_4 . In the absence of spin-orbital coupling (SOC), compound V_6Sb_4 is also a symmetry-protected Dirac nodal line semimetal. Distinguished from the open type-II nodal lines threading the Brillouin zone (BZ) in AV_6Sb_6 , V_6Sb_4 possesses closed type-I Dirac nodal rings with respect to the inverted point at the boundary of the BZ. When SOC is considered, the breaking of spin-rotation symmetry destroys the nodal rings. Strikingly, the spin Berry curvature of gapped nodal rings can lead to a large intrinsic SHE, which indicates that the V_6Sb_4 compound can create a transverse pure spin current under a longitudinal electric field [28]. Therefore, our results further expand the nonmagnetic kagome compounds for applications in spintronics accompanied by exotic quantum order.

II. COMPUTATIONAL METHODS

To investigate the electronic and topological properties of V_6Sb_4 , we performed first-principles calculations as implemented in the Vienna *ab initio* simulation package (VASP) [29] based on density functional theory (DFT) [30]. We employed the generalized gradient approximation (GGA) with Perdew-Burke-Ernzerhof formalism to describe the exchange-correlation functional [31]. The valence electron-ion interaction was treated by projector augmented-wave potentials [32]. The cutoff energy of the plane-wave basis was set to 500 eV, and the BZ was sampled using a $15 \times 15 \times 15$ Monkhorst-Pack grid [33]. To reveal the van der Waals interactions along the c -layer stacking direction, the Crimme (DFT-D3) method was used [34]. The forces on each atom were relaxed to less than 1.0×10^{-4} eV/Å. The topological classification was confirmed by the Z_2 invariant [35], which was calculated from the parity eigenvalues at the time-reversal invariant momenta (TRIM) points using the IRVSP package [36]. By projecting the Bloch states into highly symmetric atomic orbitals of Wannier functions (WF) (Sb- p , V- p , and V- d orbitals), we constructed a Wannier tight-binding (TB) Hamiltonian based on maximally localized Wannier function (MLWF) methods [37,38]. For the construction of the MLWF, a large inner-frozen window of -8.0 to 8.0 eV with respect to the Fermi level was used to calculate the intrinsic spin Hall conductivity (SHC). Then, we calculated the SHC by employing the Kubo formula in the clean limit [39,40],

$$\sigma_{\alpha\beta}^{\gamma} = e\hbar \int \frac{dk_x dk_y dk_z}{(2\pi)^3} \sum_n f_{nk} \Omega_{n,\alpha\beta}^{\gamma}(\mathbf{k}),$$

$$\Omega_{n,\alpha\beta}^{\gamma}(\mathbf{k}) = -2\text{Im} \sum_{m \neq n} \frac{\langle \psi_{nk} | j_{\alpha}^{\gamma} | \psi_{mk} \rangle \langle \psi_{mk} | v_{\beta} | \psi_{nk} \rangle}{(E_{mk} - E_{nk})^2}, \quad (1)$$

where f_{nk} is the Fermi-Dirac distribution of the n th band, the spin current operator $j_{\alpha}^{\gamma} = 1/2\{v_{\alpha}, s^{\gamma}\}$ with the spin operator s^{γ} and the velocity operator $v_{\alpha} = \frac{1}{\hbar} \frac{\partial H}{\partial k_{\alpha}}$ ($\alpha, \beta, \gamma = x, y, z$), and E_{nk} is the eigenvalue of the Bloch functions ψ_{nk} . $\Omega_{n,\alpha\beta}^{\gamma}(\mathbf{k})$ denotes the spin Berry curvature. The SHC $\sigma_{\alpha\beta}^{\gamma}$ represents the spin current j_{α}^{γ} along the α direction with spin

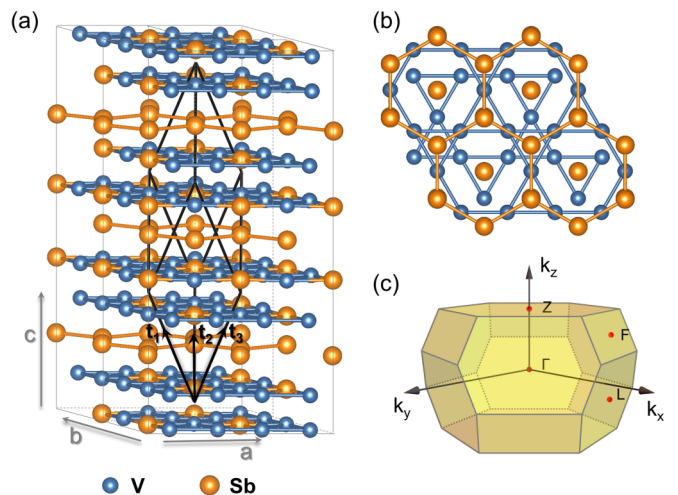


FIG. 1. (a) Crystal structure of the vanadium-based V_6Sb_4 kagome bilayer. The conventional unit cell (gray lines) in the hexagonal representation and primitive unit cell (black lines) in the rhombohedral representation are illustrated. (b) Top view of V_6Sb_4 compound. It was found that two V_3Sb bilayers were separated by two Sb (i.e., Sb2) layers. The V atoms in each V_3Sb bilayer form a kagome lattice, and the Sb (i.e., Sb1) atoms in each layer form a honeycomb lattice. (c) Bulk Brillouin zone (BZ) of a rhombohedral unit cell in which the high-symmetry points are marked.

polarization along the γ direction, which is generated by an electric field E_{β} along the β direction, that is, $j_{\alpha}^{\gamma} = \sigma_{\alpha\beta}^{\gamma} E_{\beta}$. From the Wannier TB Hamiltonian, we numerically calculated the integral of the spin Berry curvature in the momentum space to obtain the SHC based on Eq. (1), and a dense k -mesh grid of $200 \times 200 \times 200$ was adopted. It is worth noting that we employ the conventional definition of spin current in Eq. (1), which is not a conserved current. The SHC can also be calculated from the conserved spin current using the momentum space Berry curvature instead of the spin Berry curvature [41,42]. In general, these two methods would give similar characters of SHC.

III. RESULTS AND DISCUSSION

A. The crystal structure

The V_6Sb_4 compound crystallizes in a rhombohedral layered structure with space group $R\bar{3}m$ (No. 166). As shown in Fig. 1(a), its conventional unit cell in the hexagonal representation exhibits a layered structure with in-plane unit cell vectors \mathbf{a} and \mathbf{b} , and $|\mathbf{a}| = |\mathbf{b}| = a$. The stacking period of V_6Sb_4 is characterized by the out-of-plane lattice vector \mathbf{c} . Therefore, the primitive lattice vectors of the unit cell in the rhombohedral representation link the hexagonal lattice constants as

$$\mathbf{t}_1 = -\frac{a}{2}\mathbf{i} - \frac{\sqrt{3}}{6}a\mathbf{j} + \frac{c}{3}\mathbf{k}, \quad \mathbf{t}_2 = \frac{a}{2}\mathbf{i} - \frac{\sqrt{3}}{6}a\mathbf{j} + \frac{c}{3}\mathbf{k},$$

$$\mathbf{t}_3 = \frac{\sqrt{3}}{3}a\mathbf{j} + \frac{c}{3}\mathbf{k}. \quad (2)$$

As shown in Figs. 1(a) and 1(b), the $(V_3Sb)_2$ bilayer forms kagome nets of V atoms coordinated by Sb1 atoms, and

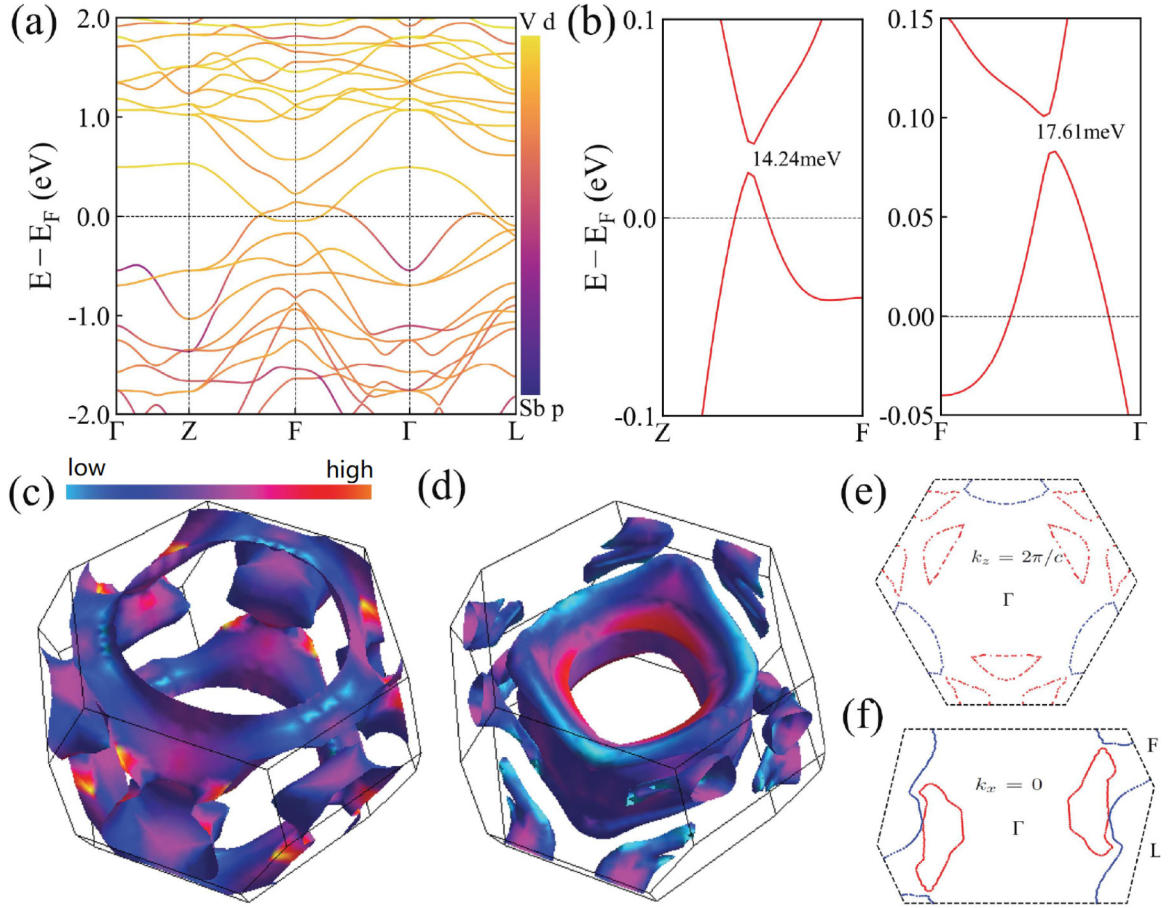


FIG. 2. Electronic band structures and Fermi surface of V_6Sb_4 . (a) Orbital resolved electronic band structures along high-symmetry paths in the absence of SOC. The yellow and blue colors represent the components of the V d and Sb p orbitals, respectively. (b) Enlarged views of band structures in the F - Z and F - Γ directions in the presence of SOC. The three-dimensional Fermi surface of (c) electron and (d) hole pockets. The color bar represents Fermi velocity. Two-dimensional slices of the Fermi surface at (e) $k_z = 2\pi/c$ and (f) $k_x = 0$. The red and blue regions denote the hole and electron pockets, respectively.

separated by the Sb2 sublattice with a honeycomb sublattice, forming a sandwiched structure. Each layer of the $(V_3Sb)_2$ bilayer is composed of a V-kagome sublattice interpenetrated with the Sb(Sb1) trigonal sublattice. The V sublattice of each layer of the $(V_3Sb)_2$ bilayer forms a kagome lattice, which is analogous to AV_3Sb_5 . The triangle sizes of the V kagome plane are divided into two unequal values induced by the breathing anisotropy, similar to Fe_3Sn_2 [43,44]. After full relaxation, the calculated lattice constants are $a = 5.42 \text{ \AA}$ and $c = 20.15 \text{ \AA}$, which are consistent with the experimental values [26]. The atom positions of the V_6Sb_4 compound are Wyckoff $6h$ of the V atom, $2c$ of the Sb1 atom, and $2c$ of the Sb2 atom. The bulk BZ was shaped by a truncated octahedron, and the time-reversal invariant momentum (TRIM) points are denoted in the BZ [see Fig. 1(c)].

B. Electronic band structures and Fermi surface

Based on first-principles calculations, we obtained the electronic band structures of the V_6Sb_4 compound and confirmed that nodal rings exist in the BZ. The band structures in the absence of the SOC along the high-symmetry direction are shown in Fig. 2(a). It was determined that band crossings

in the F - Z and F - Γ directions at $\sim 0.03 \text{ meV}$ and $\sim 0.09 \text{ meV}$ above the Fermi level, respectively, formed hole pockets. The orbital-resolved contributions are also shown in Fig. 2(a). The figure shows that the V d orbitals dominate the bands around the Fermi level. Importantly, a visible band inversion occurred at the F point, at which the occupied and unoccupied bands belong to the irreducible representations (IR) A_u and B_g of the C_{2h} group. By further checking the small groups of the BZ, we determined that the two crossing bands belong to different IR Γ_1 and Γ_2 of C_s . The mirror symmetry C_s in the k_y - k_z plane with $k_x = 0$ (i.e., M_x) was derived from the product of the I -symmetry and twofold rotational symmetry C_{2x} along the x direction, that is, $M_x = IC_{2x}$. We further calculated the energy difference between the lowest conduction band and the highest valence band in the k_y - k_z plane with $k_x = 0$, and the calculated results indicate that the two bands inverted at the F point formed continuous nodal rings (see Fig. S1 of the Supplemental Material [45]). Consequently, nodal rings with respect to mirror-reflection symmetry could be present. Notably, these nodal rings of V_6Sb_4 were protected by the coexistence of spatial inversion (I) and time-reversal (T) symmetries, although they were located in the reflection-invariant plane. For the IT -protected nodal line semimetals,

the spin-rotation symmetry enabled us to effectively treat electrons as spinless fermions with $(IT)^2 = 1$ in the absence of the SOC, corresponding to the \mathbb{Z}_2 classification for V_6Sb_4 [46]. Considering the threefold rotational symmetry C_{3z} , there were three equivalent mirror planes, and thus six nodal rings enclosed the F point in the BZ.

When the SOC effect was considered, the spin-rotation symmetry was broken, which usually destroys nodal lines protected by the space-time IT symmetry [i.e., $(IT)^2 = -1$] [46,47]. As shown in Fig. 2(b), the presence of I symmetry forces the degeneracy of two spin bands within SOC, and the previous crossing bands belong to the same IR Γ_4 of C_3 now. The DFT calculations confirmed that the band gaps are 14.2 meV along F - Z and 17.6 meV along F - Γ . At point F , the occupied and unoccupied states near the Fermi level belong to the IRs of $\Gamma_3^- \oplus \Gamma_4^-$ and $\Gamma_3^+ \oplus \Gamma_4^+$ of C_{2h} , respectively. This opposite parity indicates that the band inverted feature at F was preserved in the presence of the SOC. In this case, we can use parity eigenvalues at the time-reversal invariant momenta (TRIM) points to depict the topological features between each pair of bands near the Fermi level. As illustrated in Table S1 of the Supplemental Material [45], the calculated parity eigenvalues indicate that bands near the Fermi level exhibit a topological switch, which was expected to generate exotic quantum transport properties.

Evidently, AV_3Sb_5 exhibits rich quantum oscillations [48], such as the multiple portions of Fermi surfaces that induce a complex superposition of quantum oscillations. Here, we plotted the three-dimensional (3D) Fermi surface of the electron and hole pockets in Figs. 2(c) and 2(d), respectively, where the color bar represents the Fermi velocity. The Fermi surface exhibits a strong 2D feature with respect to the threefold rotational symmetry. The hole pockets of the Fermi surface exhibit a hollow-cylinder profile enclosed by the Γ point, while the electron pockets are close to the boundary of the BZ. Near each F point, clearly, there were two-hole pockets related to the mirror symmetry, which originate from the crossing bands of nodal rings near the Fermi level. Besides, the electron pockets have the large Fermi velocity near the boundary of the BZ, while the hole pockets have the large Fermi velocity near the center of the BZ. Hence, electron and hole pockets of V_6Sb_4 may exhibit different quantum oscillations. To further understand the properties of the Fermi surface, we provided 2D slices of the Fermi surface at $k_z = 2\pi/c$ and $k_x = 0$ in Figs. 2(e) and 2(f), respectively.

C. Spin Hall effect

Based on Eq. (1), the intrinsic SHC is derived from the spin Berry curvature of $\Omega_{n,\alpha\beta}^y(\mathbf{k})$ with the band index n in the presence of the SOC. Clearly, the band anticrossing induced by SOC can lead to large $\Omega_{n,\alpha\beta}^y(\mathbf{k})$ [49]. To obtain a large SHC, an increase in the number of band anticrossing points (i.e., band crossings without SOC) is desirable. Therefore, an assembly of continual nodal points (i.e., nodal lines) in the BZ of V_6Sb_4 can be expected to induce a strong SHE. Further, the nontrivial bands near the Fermi level can also lead to a singularity in the momentum space, which may further enlarge the SHC of V_6Sb_4 . To verify this, we calculated the band-projected plot of SHC along the high-symmetry lines

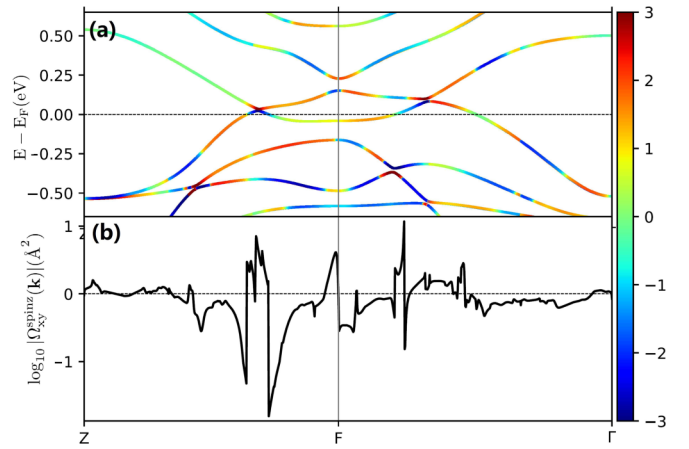


FIG. 3. (a) Band-projected SHC of the V_6Sb_4 compound along the high-symmetry lines Z - F - Γ . The color bar in (a) is the weight of the SHC projected onto each band. The magnitude of the SHC projected on each band was taken using the logarithm [40]. (b) Moment-resolved SHC along the high-symmetry lines Z - F - Γ .

Z - F - Γ , as shown in Fig. 3(a). Here, the magnitude of the SHC projected on each band was taken by the logarithm [40]. As expected, we found that the SHC was mostly concentrated near the region of the band gaps opened by SOC. In addition, we can see that the spin Berry curvature varies dramatically, which may be originated from the multiband anticrossings and nontrivial band topology switch (see Table S1 of the Supplemental Material [45]) near the Fermi level. As shown in Fig. 3(b), we calculated the k -point resolved SHC, which

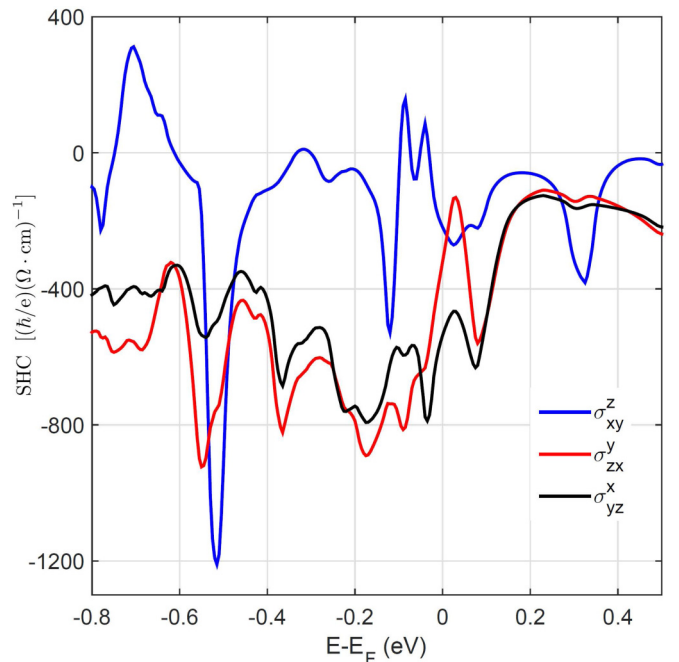


FIG. 4. SHC of V_6Sb_4 as a function of chemical potential. The independent SHC tensor elements σ_{xy}^z , σ_{zx}^y , and σ_{yz}^x are colored in blue, red, and black, respectively.

can be expressed as

$$\Omega_{xy}^{\text{spin}z}(\mathbf{k}) = \sum_n f_{n\mathbf{k}} \Omega_{n,xy}^{\text{spin}z}(\mathbf{k}). \quad (3)$$

The figure shows that the peaks around the band gaps opened by SOC significantly contributed to SHC.

After analyzing the mechanism by the band-resolved and momentum-resolved SHCs, we investigated the intrinsic SHC of $V_6\text{Sb}_4$. The SHC $\sigma_{\alpha\beta}^\gamma$ is a third-order tensor with 27 elements. The crystal structure of $V_6\text{Sb}_4$ belongs to the hexagonal lattice (space group $R\bar{3}m$, No. 166). Thus, SHE is anisotropic. The nonzero elements of the SHC depend on the space group of $V_6\text{Sb}_4$. Constrained by the crystal symmetry and time-reversal symmetry, there were only three independent nonzero elements for the $V_6\text{Sb}_4$ compound, that is, σ_{xy}^z , σ_{zx}^y , and σ_{yz}^x , which satisfy $\sigma_{xy}^z = -\sigma_{yx}^z$, $\sigma_{zx}^y = -\sigma_{xz}^y$, and $\sigma_{yz}^x = -\sigma_{zy}^x$, respectively. The SHC of $V_6\text{Sb}_4$ as a function of the chemical potential is shown in Fig. 4. Clearly, σ_{yz}^x has the largest value of approximately $537 (\hbar/e)(\Omega\text{cm})^{-1}$ at the Fermi level, which is consistent with the nodal rings lying in the k_y - k_z plane with $k_z = 0$. In comparison, σ_{xy}^z and σ_{zx}^y have values of approximately $204 (\hbar/e)(\Omega\text{cm})^{-1}$ and $357 (\hbar/e)(\Omega\text{cm})^{-1}$, respectively. Moreover, we found that the SHC varied quickly as a function of chemical potential. Because the band crossing points of nodal rings are located near but away from the Fermi level, the curve of SHC σ_{yz}^x exhibits two peak values below and above the Fermi level, that is, $788 (\hbar/e)(\Omega\text{cm})^{-1}$ at $E = E_F - 0.035$ eV and $631 (\hbar/e)(\Omega\text{cm})^{-1}$ at $E = E_F + 0.075$ eV. These values are approximate to the SHC of Weyl semimetal TaAs $\sim 781 (\hbar/e)(\Omega\text{cm})^{-1}$ [49]. Therefore, the $V_6\text{Sb}_4$ compound is a potential Dirac nodal line semimetal with a large intrinsic SHC, which could provide promising applications for spintronic devices.

IV. SUMMARY

In summary, using first-principles calculations, we theoretically investigated the band topology and the intrinsic spin Hall effect (SHE) of $V_6\text{Sb}_4$. In the absence of the SOC, this compound is a Dirac nodal line semimetal with symmetry-protected nodal rings near the Fermi level. Within the SOC, the spin-rotation symmetry breaking leads to nodal rings gapped with a small band gap. Furthermore, based on the Wannier tight-binding approach and Kubo formula, we also uncovered the large spin Hall conductivity in the $V_6\text{Sb}_4$ compound, which is up to $788 (\hbar/e)(\Omega\text{cm})^{-1}$ near the Fermi level. The large SHE is attributed to the intrinsic mechanism of spin Berry curvature. Considering that the compound $V_6\text{Sb}_4$ was recently synthesized in experiments [26], our findings can be expected to facilitate V-based kagome compounds with exotic quantum order for applications in spintronics.

ACKNOWLEDGMENTS

This work is supported by the Anhui Initiative in Quantum Information Technologies (Grant No. AHY160000), the Key Research Program of Frontier Sciences, CAS, China (Grant No. QYZDYSSWSLH021), the National Natural Science Foundation of China (Grants No. 11888101, No. 11974062, and No. 12147102), the National Key Research and Development Program of the Ministry of Science and Technology of China (Grants No. 2017YFA0303001, No. 2019YFA0704901, and No. 2016YFA0300201), the Strategic Priority Research Program of the Chinese Academy of Sciences (Grant No. XDB25000000), and the Science Challenge Project of China (Grant No. TZ2016004). The DFT calculations in this work are supported by the Supercomputing Center of University of Science and Technology of China.

-
- [1] H.-M. Guo and M. Franz, *Phys. Rev. B* **80**, 113102 (2009).
- [2] A. O'Brien, F. Pollmann, and P. Fulde, *Phys. Rev. B* **81**, 235115 (2010).
- [3] F. Pollmann, K. Roychowdhury, C. Hotta, and K. Penc, *Phys. Rev. B* **90**, 035118 (2014).
- [4] A. Rüegg and G. A. Fiete, *Phys. Rev. B* **83**, 165118 (2011).
- [5] J.-X. Yin, M. Wenlong, T. A. Cochran, X. Xu, S. S. Zhang, H.-J. Tien, N. Shumiya, C. Guangming, K. Jiang, L. Biao, S. Zhida, G. Chang, I. Belopolski, M. Daniel, M. Litskevich, Z.-J. Cheng, X. P. Yang, B. Swidler, H. Zhou, H. Lin *et al.*, *Nature (London)* **583**, 533 (2020).
- [6] Y. Zhou, K. Kanoda, and T.-K. Ng, *Rev. Mod. Phys.* **89**, 025003 (2017).
- [7] S. Yan, D. A. Huse, and S. R. White, *Science* **332**, 1173 (2011).
- [8] W.-H. Ko, P. A. Lee, and X.-G. Wen, *Phys. Rev. B* **79**, 214502 (2009).
- [9] B. R. Ortiz, L. C. Gomes, J. R. Morey, M. Winiarski, M. Bordelon, J. S. Mangum, I. W. H. Oswald, J. A. Rodriguez-Rivera, J. R. Neilson, S. D. Wilson, E. Ertekin, T. M. McQueen, and E. S. Toberer, *Phys. Rev. Mater.* **3**, 094407 (2019).
- [10] F. H. Yu, M. D. H., W. Z. Zhou, S. Q. Liu, X. K. Wen, B. Lei, J. J. Ying, and X. H. Chen, *Nat. Commun.* **12**, 3645 (2021).
- [11] H. Li, T. T. Zhang, T. Yilmaz, Y. Y. Pai, C. E. Marvinney, A. Said, Q. W. Yin, C. S. Gong, Z. J. Tu, E. Vescovo, C. S. Nelson, R. G. Moore, S. Murakami, H. C. Lei, H. N. Lee, B. J. Lawrie, and H. Miao, *Phys. Rev. X* **11**, 031050 (2021).
- [12] Z. Liang, X. Hou, F. Zhang, W. Ma, P. Wu, Z. Zhang, F. Yu, J.-J. Ying, K. Jiang, L. Shan, Z. Wang, and X.-H. Chen, *Phys. Rev. X* **11**, 031026 (2021).
- [13] Q. Yin, Z. Tu, C. Gong, Y. Fu, S. Yan, and H. Lei, *Chin. Phys. Lett.* **38**, 037403 (2021).
- [14] H. Tan, Y. Liu, Z. Wang, and B. Yan, *Phys. Rev. Lett.* **127**, 046401 (2021).
- [15] B. R. Ortiz, S. M. L. Teicher, Y. Hu, J. L. Zuo, P. M. Sarte, E. C. Schueller, A. M. Milinda Abeykoon, M. J. Krogstad, S. Rosenkranz, R. Osborn, R. Seshadri, L. Balents, J. He, and S. D. Wilson, *Phys. Rev. Lett.* **125**, 247002 (2020).
- [16] B. R. Ortiz, P. M. Sarte, E. M. Kenney, M. J. Graf, S. M. L. Teicher, R. Seshadri, and S. D. Wilson, *Phys. Rev. Materials* **5**, 034801 (2021).
- [17] X. Chen, X. Zhan, X. Wang, J. Deng, X.-B. Liu, X. Chen, J.-G. Guo, and X. Chen, *Chin. Phys. Lett.* **38**, 057402 (2021).
- [18] S. Ni, S. Ma, Y. Zhang, J. Yuan, H. Yang, Z. Lu, N. Wang, J. Sun, Z. Zhao, D. Li, S. Liu, H. Zhang, H. Chen, K. Jin,

- J. Cheng, L. Yu, F. Zhou, X. Dong, J. Hu, H.-J. Gao *et al.*, *Chin. Phys. Lett.* **38**, 057403 (2021).
- [19] Y.-X. Jiang, J.-X. Yin, M. M. Denner, N. Shumiya, B. R. Ortiz, G. Xu, Z. Guguchia, J. He, M. S. Hossain, X. Liu, J. Ruff, L. Kautzsch, S. S. Zhang, G. Chang, I. Belopolski, Q. Zhang, T. A. Cochran, D. Multer, M. Litskevich, Z.-J. Cheng *et al.*, *Nat. Mater.* **20**, 1353 (2021).
- [20] H. Chen, H. Yang, B. Hu, Z. Zhao, J. Yuan, Y. Xing, G. Qain, Z. Huang, G. Li, Y. Ye, S. Ma, S. Ni, H. Zhang, Q. Yin, C. Gong, Z. Tu, H. Lei, H. Tan, S. Zhou, C. Shen *et al.*, *Nature (London)* **599**, 222 (2021).
- [21] H. Zhao, H. Li, B. R. Ortiz, S. M. L. Teicher, T. Park, M. Ye, Z. Wang, L. Balents, S. D. Wilson, and I. Zeljkovic, *Nature (London)* **599**, 216 (2021).
- [22] F. H. Yu, T. Wu, Z. Y. Wang, B. Lei, W. Z. Zhuo, J. J. Ying, and X. H. Chen, *Phys. Rev. B* **104**, L041103 (2021).
- [23] S.-Y. Yang, Y. Wang, B. R. Ortiz, D. Liu, J. Gayles, E. Derunova, R. Gonzalez-Hernandez, L. Šmejkal, Y. Chen, S. S. P. Parkin, S. D. Wilson, E. S. Toberer, T. McQueen, and M. N. Ali, *Sci. Adv.* **6**, eabb6003 (2020).
- [24] J. Zhao, W. Wu, Y. Wang, and S. A. Yang, *Phys. Rev. B* **103**, L241117 (2021).
- [25] X. Feng, K. Jiang, Z. Wang, and J. Hu, *Sci. Bull.* **66**, 1384 (2021).
- [26] M. Shi, F. Yu, Y. Yang, F. Meng, B. Lei, Y. Luo, Z. Sun, J. He, R. Wang, T. Wu, Z. Wang, Z. Xiang, J. Ying, and X. Chen, *arXiv:2110.09782*.
- [27] Y. Yang, R. Wang, M.-Z. Shi, Z. Wang, Z. Xiang, and X.-H. Chen, *Phys. Rev. B* **104**, 245128 (2021).
- [28] J. Sinova, S. O. Valenzuela, J. Wunderlich, C. H. Back, and T. Jungwirth, *Rev. Mod. Phys.* **87**, 1213 (2015).
- [29] G. Kresse and J. Furthmüller, *Phys. Rev. B* **54**, 11169 (1996).
- [30] W. Kohn and L. J. Sham, *Phys. Rev.* **140**, A1133 (1965).
- [31] J. P. Perdew, K. Burke, and M. Ernzerhof, *Phys. Rev. Lett.* **77**, 3865 (1996).
- [32] G. Kresse and D. Joubert, *Phys. Rev. B* **59**, 1758 (1999).
- [33] H. J. Monkhorst and J. D. Pack, *Phys. Rev. B* **13**, 5188 (1976).
- [34] S. Grimme, S. Ehrlich, and L. Goerigk, *J. Comput. Chem.* **32**, 1456 (2011).
- [35] L. Fu, C. L. Kane, and E. J. Mele, *Phys. Rev. Lett.* **98**, 106803 (2007).
- [36] J. Gao, Q. Wu, C. Persson, and Z. Wang, *Comput. Phys. Commun.* **261**, 107760 (2021).
- [37] Y. S. L. I. S. A. A. Mostofi, J. R. Yates, D. Vanderbilt, and N. Marzari, *Comput. Phys. Commun.* **178**, 685 (2008).
- [38] N. Marzari, A. A. Mostofi, J. R. Yates, I. Souza, and D. Vanderbilt, *Rev. Mod. Phys.* **84**, 1419 (2012).
- [39] G. Y. Guo, Y. Yao, and Q. Niu, *Phys. Rev. Lett.* **94**, 226601 (2005).
- [40] J. Qiao, J. Zhou, Z. Yuan, and W. Zhao, *Phys. Rev. B* **98**, 214402 (2018).
- [41] J. Shi, P. Zhang, D. Xiao, and Q. Niu, *Phys. Rev. Lett.* **96**, 076604 (2006).
- [42] C. Xiao and Q. Niu, *Phys. Rev. B* **104**, L241411 (2021).
- [43] Z. Lin, J.-H. Choi, Q. Zhang, W. Qin, S. Yi, P. Wang, L. Li, Y. Wang, H. Zhang, Z. Sun, L. Wei, S. Zhang, T. Guo, Q. Lu, J.-H. Cho, C. Zeng, and Z. Zhang, *Phys. Rev. Lett.* **121**, 096401 (2018).
- [44] L. Ye, M. Kang, J. Liu, F. v. Cube, C. R. Wicker, T. Suzuki, C. Jozwiak, A. Bostwick, E. Rotenberg, D. C. Bell, L. Fu, R. Comin, and J. G. Checkelsky, *Nature (London)* **555**, 638 (2018).
- [45] See Supplemental Material at <http://link.aps.org/supplemental/10.1103/PhysRevB.105.155102> for the energy difference map between the conduction band and valence band, and the parity at TRIMs.
- [46] Y. X. Zhao, A. P. Schnyder, and Z. D. Wang, *Phys. Rev. Lett.* **116**, 156402 (2016).
- [47] Y. Kim, B. J. Wieder, C. L. Kane, and A. M. Rappe, *Phys. Rev. Lett.* **115**, 036806 (2015).
- [48] B. R. Ortiz, S. M. L. Teicher, L. Kautzsch, P. M. Sarte, N. Ratcliff, J. Harter, J. P. C. Ruff, R. Seshadri, and S. D. Wilson, *Phys. Rev. X* **11**, 041030 (2021).
- [49] Y. Sun, Y. Zhang, C. Felser, and B. Yan, *Phys. Rev. Lett.* **117**, 146403 (2016).